Chinese Chemical Letters 33 (2022) 3287–3290

Contents lists available at ScienceDirect

Chinese Chemical Letters

journal homepage: www.elsevier.com/locate/cclet

Understanding the separator pore size inhibition effect on lithium dendrite *via* phase-field simulations

Yajie Li[a], Geng Zhang[b,*], Bin Chen[a], Wei Zhao[a], Liting Sha[a], Da Wang[a], Jia Yu[c], Siqi Shi[a,c,d,**]

[a] School of Materials Science and Engineering, Shanghai University, Shanghai 200444, China
[b] Physical Science and Engineering Division, King Abdullah University of Science and Technology, Thuwal 23955-6900, Saudi Arabia
[c] Materials Genome Institute, Shanghai University, Shanghai 200444, China
[d] Zhejiang Laboratory, Hangzhou 311100, China

ARTICLE INFO

Article history:
Received 9 March 2022
Revised 14 March 2022
Accepted 15 March 2022
Available online 17 March 2022

Keywords:
Lithium-ion batteries
Pore size
Ionic distribution
Phase-field simulations
Dendrite growth

ABSTRACT

Dendrite growth in lithium-ion batteries may bring thermal run-away especially at high current densities, which remains the major bottleneck to implement safe and fast charging for portable electronic devices or electronical vehicles. Designing dendrite inhibition separators with proper pore size is considered to be one of the most promising strategies to guarantee the battery safety. However, due to the impossible observation of lithium-ion distribution under separator by experiments, the underlying dendrite inhibition mechanism is still not fully understood. Here, we apply the phase-field model, which takes the separator phase into account to construct the electrochemical system total free energy, to study the ion re-distribution behavior of porous separator and understand the pore size inhibition effect on lithium dendrite. The numerical results indicate that separator with smaller pore size is beneficial to smoother electrodeposition, since the lithium-ion concentration on the electrode surface is more uniform under denser separator pores, when their sizes is larger than the critical nucleus. The proposed model could capture the physicochemical process of electrodeposition under multiphase structures, so it could also be used to explore dendrite growth under composite electrodes and composite solid electrolytes.

The rapid development of portable electronic devices, electronical vehicles and large-scale energy storage devices calls for advanced lithium-ion batteries (LIBs) with high energy density, reliable safety, and long cycle life [1–3]. Nevertheless, lithium dendrite growth may bring poor cycle stability and thermal run-away especially at high current densities, which remains the major bottleneck to implement safe and fast charging for LIBs [4–6]. To meet the rising demand for battery safety, separators, acting as physical barriers between electrodes, have been considered to be important components in suppressing dendrite [7,8]. Many experimental researches have revealed the relation between separator structure and dendrite growth, including pore size [9–11], pore uniformity [12–16], surface coating [17–23], and electrolyte wettability [9,11,24–27]. For example, Gao *et al.* [11] fabricated polydopamine-coated polyacrylonitrile separator through spin coating and electrospinning. The fiber diameter and surface roughness of polyacrylonitrile fibers are decreased by the polydopamine coatings; thus the separator pore size is decreased and the lithium-ion flux is homogenized. Compared with polyacrylonitrile separator, batteries with polydopamine-coated polyacrylonitrile separator have more stable cycle life and better rate capability. Qin *et al.* [14] designed a porous water-based separator with uniform pore distribution, and demonstrated that it has better dendrite inhibition ability than the separator with uneven porous structure. Surface coating of separator can not only improve battery thermal stability, but also suppress dendrite growth. Yang *et al.* [10] reported a mesoporous silica-coated aluminum oxide separator. The perpendicular nanochannels of mesoporous silica films can effectively regulate the ionic flux and lead to uniform lithium deposition. The Li-Li battery with silica-coated aluminum oxide separator exhibits excellent cycling performance at ultrahigh current densities (10 mA/cm^2) for more than 1600 h of operation. Similarly, Shen *et al.* [19] applied electrospraying and polymer photopolymerization to synthesize a chitosan, polyethylene oxide, and poly(triethylene glycol dimethacrylate) coated Celgard® separator.

* Corresponding author.
** Corresponding author at: School of Materials Science and Engineering, Shanghai University, Shanghai 200444, China.
E-mail addresses: geng.zhang@kaust.edu.sa (G. Zhang), sqshi@shu.edu.cn (S. Shi).

https://doi.org/10.1016/j.cclet.2022.03.065
1001-8417/

The surface coatings provide a lithiophilic environment, which enables uniform lithium deposition, facilitates homogeneous solid electrolyte interphase layer, and thus prevents dendrite growth.

Among the above solutions, regulating separator pore size is the easiest way with lowest cost, and almost without additional weight. Eexperimental studies have shown that separators with smaller pore size can suppress dendrite growth; this is presumably attributed to the re-distribution of lithium ions by the dense pores. However, the dynamic lithium-ion distributions inside batteries cannot be directly observed by experiments, and thus the mechanisms behind the lithium inhibition behavior are still not fully understood. Hence it is necessary to apply computational method, which is neither as difficult as theoretical study nor as time-consuming and laborious as experimental study, to investigate the evolution during electrodeposition [28]. The phase-field model is a computational model which describes microstructure evolution of material systems by using functions of space and time [29,30]. During 2003–2012, the phase-field model has been developed and applied in electrodeposition by Monroe and Newman [31], Guyer *et al.* [32,33], Okajima *et al.* [34,35]. While these models assume linear kinetics, which are not applicable for systems far from equilibrium. At 2012, Liang *et al.* [36] firstly reported a nonlinear phase-field model, which takes the Butler-Volmer reaction kinetics into account, to simulate the electrode-electrolyte interface evolution during highly nonequilibrium processes. Later, they applied the nonlinear phase-field model to describe the electrodeposition process in electrochemical systems [37]. At 2015, Chen *et al.* [38] further developed the above model to investigate the dendritic patterns during the lithium electrodeposition process, and the model is first verified by comparison with the Nernst equation in one-dimensional equilibrium system. For the application of phase-field model in dendrite growth under separators, Jana *et al.* [39] applied phase-field model to explore the effect of pore size on dendrite growth, and identified four regimes of dendrite growth: suppression regime, permeable regime, penetration regime, and short circuit regime. However, this study ignored the lithium-ion concentration during electrodeposition, which is important to understand dendrite growth mechanism.

In this paper, the influence of separator pore size on dendrite growth is studied by the phase-field model using self-written MATLAB code. This extended model takes the separator phase into account to construct the total free energy of the electrochemical system. The simulation results are firstly compared with previous studies conducted by integrated software to check validity of the model and accuracy of the code. Then we study the ion redistribution behavior of porous separator and the pore size inhibition effect on lithium dendrite.

Generally, the simulations for electrochemical dendrite growth include the following steps: (1) constructing the total free energy of the electrochemical system, (2) numerically solving the evolution equations of all fields with MATLAB, and (3) visualizing the simulation results. The figures of the phase-fields, ion concentrations, and electric potential at different times can be obtained from visualization of the numerical solution. The flow chart of the code is shown in Fig. 1.

We introduce two phase-field variables ξ and ϕ (ranging from 0 to 1) and a concentration set c_i (i=Li, Li^+ and anion A^{m-}) to describe the system. ($\xi = 1, \phi = 0$) denotes the electrode, ($\xi = 0, \phi = 1$) denotes the separator, and ($\xi = 0, \phi = 0$) denotes the electrolyte. The total free energy of the system can be expressed as

$$F = \int_V \left[f_{ch}(\xi, \phi, \{c_i\}) + f_{grad}(\nabla\xi) + f_{elec}(\{c_i\}, \Phi) \right] dV \quad (1)$$

where Φ is the electric potential, f_{ch}, f_{grad} and f_{elec} are the Helmholtz free energy density, gradient energy density, and electrostatic energy density, respectively.

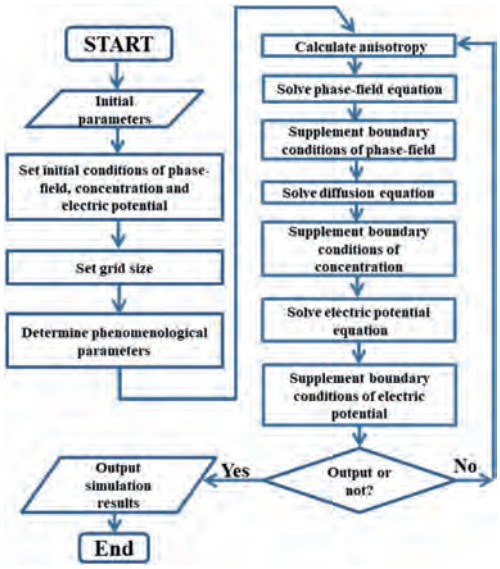

Fig. 1. Flow chart of phase-field simulation code.

The chemical free energy density is expressed as follows:

$$f_{ch}(\xi, \phi, \{c_i\}) = \sum_i c_i \mu_i^\circ + RT\left(c_{Li^+} \ln \frac{c_{Li^+}}{c_0} + c_{A^{m-}} \ln \frac{c_{A^{m-}}}{c_0}\right) + W_{01}\xi^2(1-\xi)^2 + W_{02}\phi^2(1-\phi)^2 + W_{12}\xi^2\phi^2 \quad (2)$$

where μ_i° is the reference chemical potential of component i, R is the molar gas constant, and T is the temperature. The last three terms of the right side represents interphase barrier potentials, with W_{01}, W_{02} and W_{12} being constants. The gradient energy density is expressed as:

$$f_{grad}(\nabla\xi) = \frac{1}{2}\kappa_1[1 + \delta\cos(\omega\theta)](\nabla\xi)^2 \quad (3)$$

where κ_1 is the gradient energy coefficients, δ is the anisotropic strength, ω is the anisotropic mode, θ is the angle between the interface normal vector and the reference axis. The electrostatic energy density is expressed as

$$f_{elec}(c_i, \varphi) = \sum_i z_i F c_i \varphi \quad (4)$$

where F is Faraday's constant and z_i is the valence. The electrochemical reaction rate can be expressed from the Butler-Volmer equation. The evolution equations for ξ and ϕ can be described as:

$$\frac{\partial\xi}{\partial t} = -L\frac{\delta f}{\delta\xi} - R_\eta h'(\xi)\left(e^{\frac{(1-\alpha)F\eta}{RT}} - \frac{c_{Li^+}}{c_0}e^{\frac{-\alpha F\eta}{RT}}\right) \quad (5)$$

$$\frac{\partial\phi}{\partial t} = 0 \quad (6)$$

where L is the interfacial mobility between the electrode and separator, R_η is the reaction constant, α and 1-α are the charge-transfer coefficients, c_0 is the initial concentration of the electrolyte, $h(\xi) = \xi^3(6\xi^2 - 15\xi + 10)$ is an interpolating function. The overpotential is defined as $\eta = \Phi - \Phi_0$, Φ is the electric potential of Li metal anode, Φ_0 is the equilibrium potential without electric current. The evolution equation of Li^+ concentration is

$$\frac{\partial c_{Li^+}}{\partial t} = \nabla\cdot\left(D_{eff}\nabla c_{Li^+} + D_{eff}c_{Li^+}\frac{F}{RT}\nabla\Phi\right) - K\frac{\partial\xi}{\partial t} \quad (7)$$

where $D_{eff} = (h(\xi) + h(\phi))D_{Li} + [1 - h(\xi) - h(\phi)]D_e$ is the effective diffusion coefficient, D_{Li^+} is the diffusion coefficient of Li^+ in the electrolyte, D_e is the diffusion coefficient of Li^+ in the electrode, and K is the accumulation constant. The evolution equation

Table 1
Parameters in the phase-field model.

Parameters	Symbol	Value
Interfacial mobility	L_1	2.5×10^{-6} m^3 J^{-1} s^{-1}
Reaction constant	R_η	1 s^{-1}
Gradient energy coefficient 1	κ_1	4.17×10^{-5} J/m
Anisotropic strength	δ	0.05
Anisotropic mode number	ω	4
Barrier height 1	W_{01}	1.334×10^7 J/m^3
Barrier height 2	W_{02}	1.334×10^7 J/m^3
Barrier height 3	W_{12}	1.334×10^7 J/m^3
Diffusion coefficient of Li^+ in electrolyte	D_{Li}	3.68×10^{-13} m^2/s
Diffusion coefficient of Li^+ in electrode	D_e	3.68×10^{-10} m^2/s
Initial Li^+ concentration in electrolyte	c_0	1×10^3 mol/m^3
Charge transfer coefficient	α	0.5
Electric conductivity of electrolyte	σ_{Li}	6.3×10^7 S/m
Electric conductivity of electrode	σ_e	2.67 S/m
Accumulation constant	K	1.92×10^3 mol/m^3
Temperature	T	298.15 K

of electrostatic potential is described by the law of charge conservation:

$$\nabla \cdot (\sigma_{\text{eff}} \nabla \Phi) = F c_{\text{Li}} \frac{\partial \xi}{\partial t} \tag{8}$$

where $\sigma_{\text{eff}} = h(\xi)\sigma_{\text{Li}} + [1 - h(\xi)]\sigma_e$ is the effective electric conductivity, σ_{Li} and σ_e are the electric conductivity of electrode and electrolyte, respectively.

The numerical solutions of Eqs. 5–8 are obtained by using the finite difference method on MATLAB. The simulation is conducted in a two-dimensional region with a size of 16×16 μm^2, and the grid spacing is 0.08 μm. The parameters used are listed in Table 1. The adiabatic boundary condition is used for the four boundaries of the phase-field variable, and left and right boundaries of the concentration and electric potential. The top and bottom boundaries of concentration are set as 1 and 0, respectively. The top and bottom boundaries of electric potential are set as 0 V and −0.7 V, respectively.

In order to verify the feasibility of the electrochemical phase-field model, we conducted a simulation without separator and compared the results with the previous work. As shown in Fig. 2a, the blue area represents the electrolyte. The upper and lower boundary conditions are set as the Dirichlet boundary conditions, and three initial semicircular nuclei are set on the electrode. The evolutions of phase-field variable (ξ), Li^+ concentration (c_{Li^+}) and electrical potential (Φ) from 0 to 2 s are shown in Fig. 2. Due to the tetragonal crystal structure of Li (BCC), four equal branches will appear. Since the bottom margin of the simulation region represents the solid electrode phase, there are only three branches growing towards the electrolyte phase in electrodeposition (Fig. 2b) [40]. The concentration/electric potential gradient at the interface is the electrodeposition driving force.

From Figs. 2b–d, it can be observed that the growth rate at the dendrite tip is much faster than that at the bottom, since the diffusion path of lithium ions is shorter for the tips [41]. When the secondary dendrite get in contact with each other, the length of the secondary dendrite between two nucleation sites is much less than that of the outer secondary dendrite due to the competition between adjacent dendrite. This is consistent with the results in previous work through COMSOL or MOOSE [38]. The ionic concentration and potential in electrolyte is also in good agreement with the work of Chen *et al.* [38,41,42]. These simulation results show validity of the proposed electrochemical phase-field model.

Next, the effect of pore size on Li dendrite growth is explored by six separator pore sizes (0.21, 0.42, 0.84, 1.05, 2.1 and 6 μm). At 5 s, the Li dendrite morphology under different pore sizes is shown in Figs. 3a–f. The line chart of maximum dendrite length with respect to pore size is plotted in Fig. 3g. It can be observed

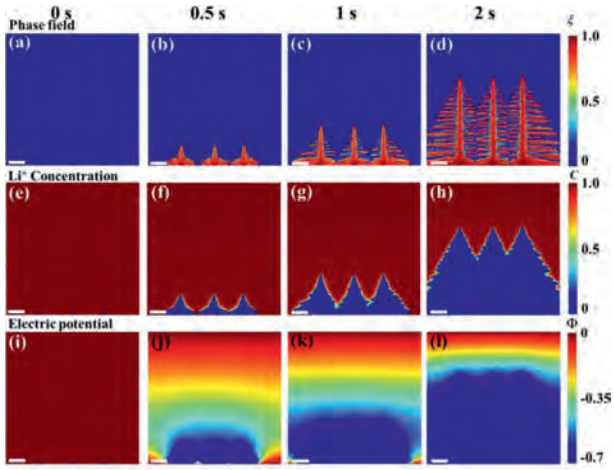

Fig. 2. Evolution of (a–d) phase-field variable, (e–h) Li^+ concentration, and (i–l) electric potential without separator. Scale bar: 2 μm.

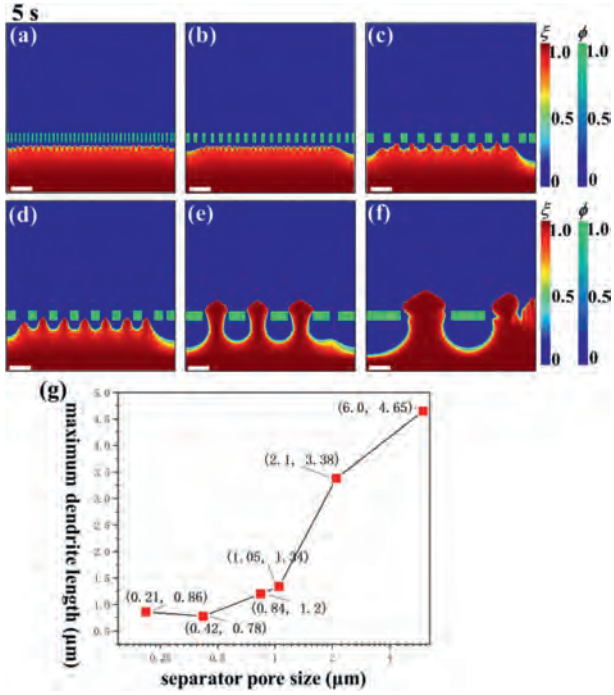

Fig. 3. Phase-field variable at 5 s under different pore sizes: (a) 0.21 μm, (b) 0.42 μm, (c) 0.84 μm, (d) 1.05 μm, (e) 2.1 μm, (f) 6 μm, and (g) maximum dendrite length *versus* pore sizes. Scale bar: 2 μm.

that with the increase of pore size, the maximum height of dendrite increases gradually. From Figs. 3e and f, when the pore size is too large, the dendrite can easily puncture the separator; thus inducing a short circuit of the battery. However, the pore size is not better if too small. By comparing Figs. 3a and b, it is seen that the dendrite length under pore size of 0.21 μm is higher than that of 0.42 μm, because dendrite can go through the separator if the pore size is close to the critical nuclei [39].

To further analyze the mechanism behind dendrite growth, we plotted the lithium-ion concentration under different pore sizes from 0 to 5 s, as shown in Fig. 4. The initial lithium-ion concentrations under different pore sizes are all the same. At 1 s, lithium ions are consumed due to electrochemical reaction and deposited on the electrode, resulting in the low lithium-ion concentration near the electrode. Concentration difference drives lithium-ion migration from the electrolyte to the anode. Lithium ions can pass

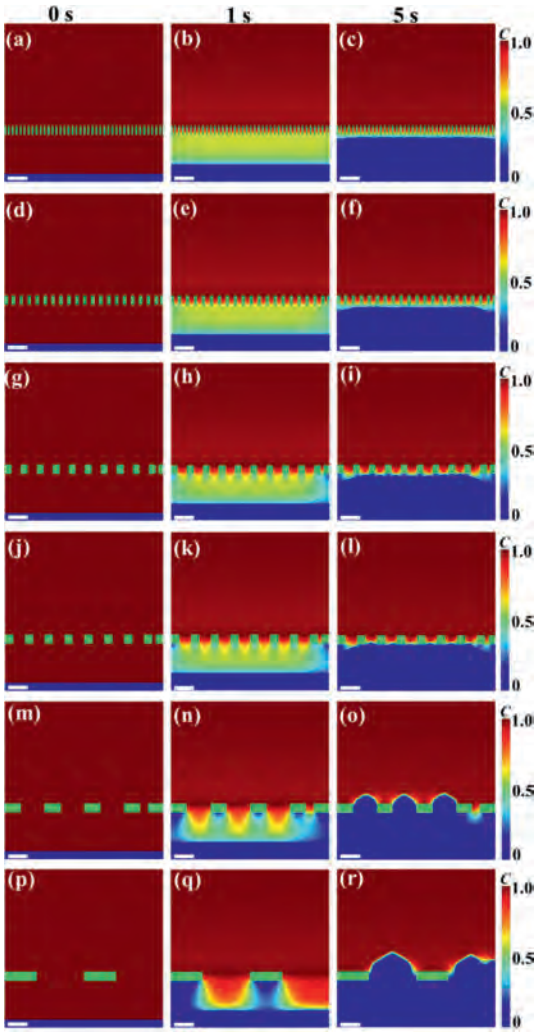

Fig. 4. Lithium-ion concentration at 0, 1 and 5 s under different pore sizes: (a–c) 0.21 μm, (d–f) 0.42 μm, (g–i) 0.84 μm, (j–l) 1.05 μm, (m–o) 2.1 μm, and (p–r) 6 μm. Scale bar: 2 μm.

through the separator pores but cannot pass through the polymer matrix of the separators. For maintaining the same porosity, when the pore size increases, the corresponding polymer matrix area (green strip area) also increases. Therefore, if the matrix area is too large, the lithium-ion concentration under it will be reduced obviously, resulting in uneven distribution of lithium-ions, as shown in Figs. 4n and q. The uneven distribution of lithium ions aggravates the tip effect, which in turn increases ionic heterogeneity and promotes dendrite growth.

In this paper, an electrochemical phase-field model and its corresponding MATLAB code are developed to explore the electrodeposition behavior under separators with different pore size. The results indicate that separators with smaller pore size are beneficial to smoother electrodeposition. While when the pore size decreased close to the critical nuclei, the dendrite growth will be promoted instead. This simulation provides significant strategies to material scientists for developing separators with optimum dendrite inhibition effect.

Declaration of competing interest

The authors declare that they have no known competing financial interests or personal relationships that could have appeared to influence the work reported in this paper.

Acknowledgments

This work was supported by the National Natural Science Foundation of China (Nos. 52102280, U2030206, 11874254, 51622207), Shanghai Pujiang Program (No. 2019PJD016), Foundation of China Academy of Engineering Physics-Key Laboratory of Neutron Physics (No. 2019BB07), and Scientific Research Project of Zhijiang Laboratory (No. 2021PE0AC02). It was also supported by funding from King Abdullah University of Science and Technology (KAUST).

References

[1] G.E. Blomgren, J. Electrochem. Soc. 164 (2017) A5019–A5025.
[2] T. Kim, W. Song, D.Y. Son, et al., J. Mater. Chem. A 7 (2019) 2942–2964.
[3] D. Zhang, L. Li, W. Zhang, et al., Chin. Chem. Lett. (2022) doi:10.1016/j.cclet.2022.01.015.
[4] P. Arora, Z. Zhang, Chem. Rev. 104 (2004) 4419–4462.
[5] A. Mauger, M. Armand, C. Julien, et al., J. Power Sources 353 (2017) 333–342.
[6] M. Zhang, R. Liu, Z. Wang, et al., Chin. Chem. Lett. 31 (2020) 1217–1220.
[7] K. Liu, Y.Y. Liu, D.C. Lin, et al., Sci. Adv. 4 (2018) eaas9820.
[8] D. Ren, X. Feng, L. Liu, et al., Energy Storage Mater. 34 (2021) 563–573.
[9] L. Ma, R. Chen, Y. Hu, et al., Energy Storage Mater. 14 (2018) 258–266.
[10] J. Yang, C.Y. Wang, C.C. Wang, et al., J. Mater. Chem. A 8 (2020) 5095–5104.
[11] Y. Gao, X. Sang, Y. Chen, et al., J. Mater. Sci. 55 (2020) 3549–3560.
[12] Y. He, Z. Chang, S. Wu, et al., Adv. Energy Mater. 8 (2018) 1802130.
[13] X. Wu, N. Liu, Z. Guo, et al., Energy Storage Mater. 28 (2020) 153–159.
[14] Y. Qin, P. Liu, Q. Zhang, et al., Small 16 (2020) 2003106.
[15] J. Cannarella, C.B. Arnold, J. Electrochem. Soc. 162 (2015) A1365–A1373.
[16] R. Pan, R. Sun, Z. Wang, et al., Nano Energy 55 (2019) 316–326.
[17] W.K. Shin, A.G. Kannan, D.W. Kim, ACS Appl. Mater. Interfaces 7 (2015) 23700–23707.
[18] C.Z. Zhao, P.Y. Chen, R. Zhang, et al., Sci. Adv. 4 (2018) eaat3446.
[19] L. Shen, X. Liu, J. Dong, et al., J. Energy Chem. 52 (2021) 262–268.
[20] L. Xu, X.Y.D. Ma, W. Wang, et al., J. Mater. Chem. A 9 (2021) 3409–3417.
[21] J.W. Lee, A.M. Soomro, M. Waqas, et al., Int. J. Energy Res. 44 (2020) 7035–7046.
[22] M. Yang, Y. Ji, Y. Dong, et al., Chin. Chem. Lett. (2022) doi:10.1016/j.cclet.2021.12.079.
[23] P.J.H. Kim, V.G. Pol, ACS Appl. Mater. Interfaces 11 (2019) 3917–3924.
[24] H. Zheng, Y. Xie, H. Xiang, et al., Electrochim. Acta 270 (2018) 62–69.
[25] Y. Wang, Nano Micro Lett. 13 (2021) 1–3.
[26] Y. Xie, H. Xiang, P. Shi, et al., J. Membr. Sci. 524 (2017) 315–320.
[27] J.Y. Kim, D.O. Shin, K.M. Kim, et al., Sci. Rep. 9 (2019) 1–7.
[28] S.Q. Shi, J. Gao, Y. Liu, et al., Chin. Phys. B 25 (2015) 018212.
[29] Q. Wang, G. Zhang, Y. Li, et al., Npj Comput. Mater. 6 (2020) 1–8.
[30] G. Zhang, Q. Wang, L.T. Sha, et al., Acta Phys. Sin. 69 (2020) 226401.
[31] C. Monroe, J. Newman, J. Electrochem. Soc. 150 (2003) A1377.
[32] J.E. Guyer, W.J. Boettinger, J.A. Warren, et al., Phys. Rev. E 69 (2004) 021603.
[33] J.E. Guyer, W.J. Boettinger, J.A. Warren, et al., Phys. Rev. E 69 (2004) 021604.
[34] Y. Okajima, Y. Shibuta, T. Suzuki, Comput. Mater. Sci. 50 (2010) 118–124.
[35] Y. Shibuta, Y. Okajima, T. Suzuki, Sci. Technol. Adv. Mater. 8 (2007) 511.
[36] L. Liang, Y. Qi, F Xue, et al., Phys. Rev. E 86 (2012) 051609.
[37] L. Liang, L.Q. Chen, Appl. Phys. Lett. 105 (2014) 263903.
[38] L. Chen, H.W. Zhang, L.Y. Liang, et al., J. Power Sources 300 (2015) 376–385.
[39] A. Jana, D.R. Ely, R.E. García, J. Power Sources 275 (2015) 912–921.
[40] V. Yurkiv, T. Foroozan, A. Ramasubramanian, et al., Electrochim. Acta 265 (2018) 609–619.
[41] Z. Hong, V. Viswanathan, ACS Energy Lett. 3 (2018) 1737–1743.
[42] R. Zhang, X. Shen, X.B. Cheng, et al., Energy Storage Mater. 23 (2019) 556–565.